

Weak self-interactions of globular proteins studied by small-angle X-ray scattering and structure-based modeling

Shuji Kaieda¹, Mikael Lund², Tomas S. Plivelic³, and Bertil Halle¹

¹*Department of Biophysical Chemistry, Lund University, Lund, Sweden*

²*Department of Theoretical Chemistry, Lund University, Lund, Sweden*

³*MAX IV Laboratory, Lund University, Lund, Sweden*

We investigate protein–protein interactions in solution by small-angle X-ray scattering (SAXS) and theoretical modeling. The structure factor for solutions of bovine pancreatic trypsin inhibitor (BPTI), myoglobin (Mb), and intestinal fatty acid-binding protein (IFABP) is determined from SAXS measurements at multiple concentrations, from Monte Carlo simulations with a coarse-grained structure-based interaction model, and from analytic approximate solutions of two idealized colloidal interaction models without adjustable parameters. By combining these approaches, we find that the structure factor is essentially determined by hard-core and screened electrostatic interactions. Other soft short-ranged interactions (van der Waals and solvation-related) are either individually insignificant or tend to cancel out. The structure factor is also not significantly affected by charge fluctuations. For Mb and IFABP, with small net charge and relatively symmetric charge distribution, the structure factor is well described by a hard-sphere model. For BPTI, with larger net charge, screened electrostatic repulsion is also important, but the asymmetry of the charge distribution reduces the repulsion from that predicted by a charged hard-sphere model with the same net charge. Such charge asymmetry may also amplify the effect of shape asymmetry on the protein–protein potential of mean force.

1. Introduction

Protein–protein interactions govern the functional assembly of supramolecular structures^{1,2} as well as the dysfunctional aggregation of misfolded proteins.³ Weak protein–protein interactions also determine the thermodynamics and phase behavior of concentrated protein solutions,⁴ of relevance for optimizing protein crystallization⁵ and for understanding how proteins behave in the crowded cytoplasm.⁶ Fundamental progress in these areas requires a quantitative understanding of how proteins interact with themselves in solution. Specifically, we need to know the effective solvent-averaged protein–protein interaction energy or potential of mean force, $w(r)$.

Much of the available information about protein–protein interactions in solution has come from scattering experiments via the osmotic second virial coefficient, B_{22} , and the structure factor, $S(q)$.^{7–16} Whereas B_{22} is an integral measure of the pair interaction, $S(q)$ is the Fourier transform of the isotropically averaged protein–protein pair correlation induced by the interactions.¹⁷ Extraction of $w(r)$ from $S(q)$ is a nontrivial problem without a unique solution.¹⁸ Typically, a parameterized interaction model, $w(r; a, b, \dots)$, is postulated and $S(q)$ is computed by molecular simulation^{9,11,13} or by an approximate integral equation theory.^{7,8,10,12,14–16} The model parameters a, b, \dots are then optimized by comparing the computed $S(q)$ with that determined by small-angle X-ray (SAXS) or neutron (SANS) scattering.

The interaction models used in this context may be classified as colloidal or structure-based. Colloidal interaction models are typically^{7,8,10,13–15} based

on the Derjaguin–Landau–Verwey–Overbeek (DLVO) potential,¹⁹ often complemented with phenomenological short-range contributions.²⁰ In the DLVO model, the protein is described as a uniformly surface-charged sphere embedded in a dielectric continuum. Such highly idealized models have the virtue of simplicity but cannot do full justice to protein–protein interactions.^{21–26} At the short and intermediate protein–protein separations, the irregular shape and the discrete and asymmetric charge distribution of real proteins cannot be ignored. Structure-based interaction models explicitly incorporate such structural features, either at atomic resolution or at a coarse-grained level. For computational expediency, the solvent is treated as a dielectric continuum; solvation-related interaction terms of a phenomenological nature are therefore sometimes included in the model. While this approach has been used extensively to compute B_{22} ,^{27–33} relatively few studies have reported $S(q)$ calculations with structure-based interaction models.^{29,31}

Here we report the structure factor $S(q)$, determined by SAXS, for aqueous solutions of three globular proteins: bovine pancreatic trypsin inhibitor (BPTI), equine skeletal muscle myoglobin (Mb), and rat intestinal fatty acid-binding protein (IFABP). To extract information about the protein–protein interactions, we use Metropolis Monte Carlo (MC) simulations to compute $S(q)$ for these solutions based on a coarse-grained structure-based (CGSB) interaction model with the individual amino acid residues as interaction sites.²⁸ This implicit solvent model incorporates excluded volume, van der Waals (vdW) attraction, and screened Coulomb interactions, and the charges of the ionizable residues are

allowed to fluctuate. To gain further insight, we compare the experimental and CGSB $S(q)$ with the (analytic) structure factors for two colloidal interaction models: the hard-sphere fluid in the Percus–Yevick (PY) approximation^{34,35} and the hard-sphere Yukawa (HSY) fluid in the modified penetrating-background corrected rescaled mean spherical approximation (MPB-RMSA).^{36,37}

With only excluded volume and screened Coulomb interactions (no vdW attraction or other soft short-range interactions) and without any adjustable parameters, the CGSB model reproduces the experimental $S(q)$ nearly quantitatively for all three proteins within the q range 0.5–3.0 nm⁻¹ accessed by the MC simulations. For Mb and IFABP, which were examined near isoelectric pH, the hard-sphere model predicts essentially the same $S(q)$ as does the CGSB model in this q range. For the more highly charged BPTI, neither the hard-sphere model nor the charged hard-sphere model can reproduce the experimental $S(q)$. The implications of these findings are discussed.

2. Materials and Methods

2.1. SAXS Experiments

Protein solutions for SAXS measurements were prepared by dissolving lyophilized BPTI, Mb, or IFABP, purified and desalted as described,³⁸ in MilliQ water. After adjusting pH by adding HCl or NaOH, the solutions were centrifuged at 13000 rpm for 3 min to remove any insoluble protein. No buffers were used and the only electrolyte present is the counterions and a small amount of added salt (from pH adjustment) in the case of Mb. Relevant characteristics of the investigated protein solutions are summarized in Table 1.

SAXS measurements were performed at the MAX-lab synchrotron beamline I911-4, equipped with a PILATUS 1M detector (Dectris).⁴¹ The scattering vector q range ($q = 4\pi/\lambda \sin \theta$, where $\lambda = 0.91$ Å is the X-ray wavelength and 2θ is the scattering angle) was calibrated with a silver behenate sample. All measurements were performed on samples in flow-through cells at 20°C with an exposure time of 1 min. The effect of radiation damage did not exceed the experimental noise. Reported scattering profiles $I(q)$ were obtained as the difference of the azimuthally averaged 2D SAXS images from protein solution and solvent (MilliQ water).

2.2. SAXS Data Analysis

For a solution of N_P protein molecules of volume V_P contained in a volume V , the scattering intensity $I(q)$ in the decoupling approximation, where the orientation of a protein molecule is taken to be independent of its position and the configuration of other protein molecules, can be factorized as^{42–44}

$$I(q) = n_P (V_P \Delta\rho)^2 P(q) S(q), \quad (1)$$

where $n_P = N_P/V$ is the protein number density, $\Delta\rho$ is the protein–solvent electron density difference (the scattering

Table 1. Characteristics of SAXS Samples

protein	w_P (mg/ml)	C_P (mM)	ϕ_P (%) ^a	pH	Z_P ^b	C_{salt} (mM)
BPTI	1.99	0.305	0.143	4.0	+7.4	0
	9.75	1.50	0.702	4.0	+7.4	0
	39.9	6.12	2.87	4.1	+7.2	0
	101	15.5	7.27	4.1	+7.2	0
Mb	1.32	0.0752	0.0979	6.8	+3.2	0.188
	8.43	0.480	0.625	6.8	+3.2	1.20
	29.0	1.65	2.15	6.8	+3.2	4.13
IFABP	7.77	0.501	0.567	7.0	+0.2	0
	15.5	1.00	1.13	7.0	+0.2	0
	31.0	2.00	2.26	7.0	+0.2	0
	62.0	4.00	4.53	7.0	+0.2	0

^a The protein volume fraction was obtained as $\phi_P = n_P V_P$, with n_P being the protein number density and V_P the protein (partial) volume (see text).

^b Net protein valency, calculated with experimental pK_a values when available (Asp, Glu, Lys, Tyr, and N- and C-termini for BPTI³⁹ and His for Mb⁴⁰) and with standard pK_a values in proteins otherwise (C-terminus, 2.5; Asp, 3.65; Glu, 4.45; His, 6.5; N-terminus, 8.0; Tyr, 10.0; Lys, 10.6; Arg, 12.5).

contrast), $P(q)$ is the form factor, and $S(q)$ is the structure factor. Because of the non-spherical protein shape, Eq. (1) should involve an effective structure factor $\bar{S}(q)$, which, however, differs insignificantly from $S(q)$ under the conditions of the present study. The form factor represents the scattering from an isolated protein molecule,

$$P(q) = \left\langle \left| \frac{1}{V_P} \int_{V_P} d\mathbf{r} \exp(-i\mathbf{q} \cdot \mathbf{r}) \right|^2 \right\rangle, \quad (2)$$

whereas the structure factor reflects intermolecular pair correlations,

$$S(q) = \sum_{k=1}^{N_P} \langle \exp[-i\mathbf{q} \cdot (\mathbf{r}_1 - \mathbf{r}_k)] \rangle. \quad (3)$$

In Eqs. (2) and (3), $\langle \dots \rangle$ signifies an equilibrium configurational average.

According to Eq. (1), the structure factor, $S(q; n_P)$, at a protein concentration n_P can be obtained by dividing the concentration-normalized intensity, $I(q; n_P)/n_P$, by the same quantity measured at a sufficiently low concentration, n_P^0 , that $S(q; n_P^0) \equiv 1$. We shall refer to $I(q; n_P^0)/n_P^0 = (V_P \Delta\rho)^2 P(q)$ as the apparent form factor (AFF). As described in more detail elsewhere,³⁸ the AFF for each protein was constructed by merging concentration-normalized SAXS profiles from two different protein concentrations (the highest and the lowest in Table 1) and by smoothing the merged profile. The low q part of the AFF, where the SAXS profile is sensitive to protein–protein correlations, originates from the dilute solution with $S(q) \approx 1$, whereas the high q part, which reflects intraprotein correlations, is derived from a concentrated solution with better signal-to-noise.

Table 2. Characteristics of Simulated Solutions

protein	PDB	$N_{\text{res}}^{\text{a}}$	pH	C_{P} (mM)	Z_{P}^{b}	κ^{-1} (nm)	$r_{\text{C}}\kappa$
BPTI	1bpi ⁴⁵	58	4.1	1.50	+6.3	4.37	5
				6.12	+6.6	2.16	5
				15.5	+7.0	1.36	5
Mb	1wla ⁴⁶	153	6.8	0.480	+2.0 ^c	13.6	2
				1.65	+2.1 ^c	7.29	2
IFABP	1ifc ⁴⁷	131	7.0	1.00	-0.021	96.3	0.1
				2.00	-0.021	68.1	0.1
				4.00	-0.017	48.1	0.1

^a Number of residues per protein. The number of interaction sites is $N_{\text{res}} + 2$.

^b Average net protein valency determined from the simulation.

^c The fixed valency of the heme group in Mb was set to +1.

2.3. CGSB Interaction Model and MC Simulation

In the CGSB interaction model, each amino acid residue (plus the terminal amino and carboxyl groups) is represented by an isotropic interaction site, placed at the center-of-mass of the corresponding residue in the crystal structure of the real protein (Fig. 1). (For simplicity, we shall refer to these interaction sites as residues.) The effective energy of interaction between residues i and j , separated by a distance r_{ij} , is taken to be

$$u(r_{ij}) = k_{\text{B}}T\lambda_{\text{B}} \frac{z_i z_j}{r_{ij}} e^{-\kappa r_{ij}} + 4\varepsilon \left[\left(\frac{\sigma_{ij}}{r_{ij}} \right)^{12} - \left(\frac{\sigma_{ij}}{r_{ij}} \right)^6 \right] + \delta_{ij}(r_{\text{C}}). \quad (4)$$

The first term describes the electrostatic interaction in the Debye-Hückel approximation. Here, $\lambda_{\text{B}} = 0.71$ nm is the Bjerrum length for water at 20°C, $\kappa = (4\pi\lambda_{\text{B}}|Z_{\text{P}}|n_{\text{P}})^{1/2}$ is the inverse Debye screening length determined by the counterions (no added salt) of the protein with net charge valency Z_{P} , and $z_i = 0$ or ± 1 is the valency of residue i . The second term in Eq. (4), a Lennard-Jones (LJ) potential with well depth ε and $\sigma_{ij} = (\sigma_i + \sigma_j)/2$, describes exchange repulsion and vdW attraction. The vdW diameter σ_i was fixed by the residue molar mass, M_i , according to $\sigma_i = [6M_i/(\pi\rho)]^{1/3}$ with $\rho = 1$ g mol⁻¹ Å⁻³. (Varying the density ρ by $\pm 20\%$ has negligible effect on the structure factor.) Finally, in the third term of Eq. (4), $\delta_{ij}(r_{\text{C}})$ shifts the pair potential to zero at a spherical cut-off distance r_{C} in the rang 0.1–5 κ^{-1} (4.8–27.2 nm). Relevant characteristics of the simulated protein solutions are collected in Table 2.

MC simulations were performed at 293 K in the NVT ensemble with fluctuating protein charges (constant pH) using the Faunus framework.⁴⁸ The cubic simulation box, with periodic boundary conditions, contained $N_{\text{P}} = 500$ rigid, coarse-grained protein molecules and the box volume was adjusted to match the experimental protein concentrations (Table 2 and Fig. 2). Configurational space, that is, the position and orientation of each protein molecule and the protonation state of each ionizable group, was sampled by the conventional Metropolis algorithm⁴⁹ using the following

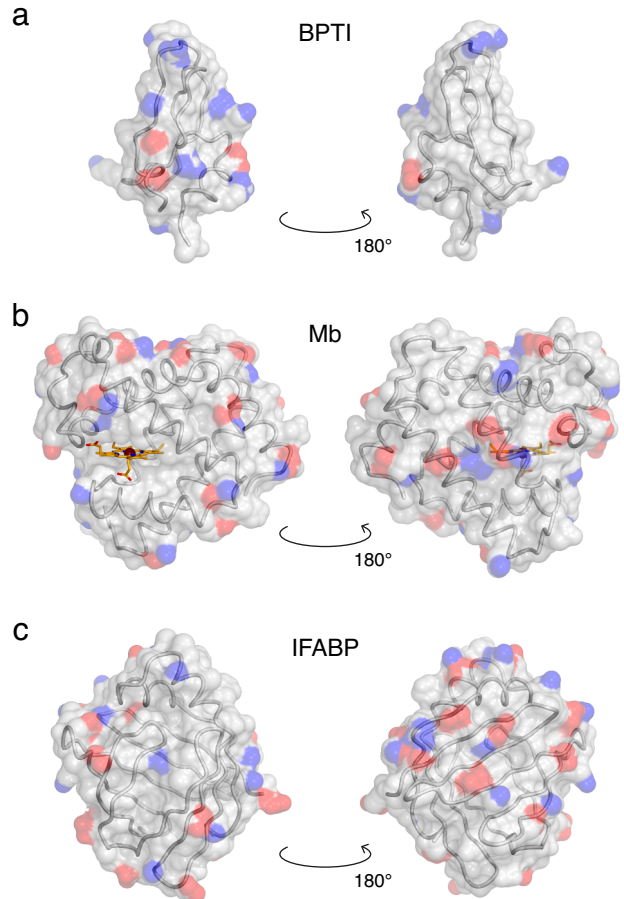


Figure 1. Crystal structures of BPTI (a; PDB ID 1bpi⁴⁵), Mb (b; 1wla⁴⁶), and IFABP (c; 1ifc⁴⁷). Backbone and surface representations are superimposed and the heme group of Mb is shown in stick representation. The protein surfaces are colored red or blue at the positions of Asp and Glu O atoms and Lys and Arg N atoms, respectively. The figure was prepared with CueMol (<http://www.cuemol.org>).

energy function,

$$U = \sum_i \sum_{j>i} u(r_{ij}) + k_{\text{B}}T \ln 10 \sum_n \alpha_n (\text{pH} - \text{p}K_{\text{a},n}^{\circ}). \quad (5)$$

In the first term, $u(r_{ij})$ is the pair potential from Eq. (4) and the double sum runs over all pairs of residues (in the same or in different protein molecules). In the second term, which ensures that the fluctuating charges conform to a Boltzmann distribution,^{50,51} the sum runs over all ionizable residues and $\alpha_n = 1$ or 0 for residues in protonated and deprotonated forms, respectively. The intrinsic (in the absence of electrostatic interactions) $\text{p}K_{\text{a},n}^{\circ}$ was taken to be 3.8 (C-terminus), 4.0 (Asp), 4.4 (Glu), 6.3 (His), 7.5 (N-terminus), 9.6 (Tyr), 10.4 (Lys), or 12.0 (Arg). Shifts in the apparent acid dissociation constant, $\text{p}K_{\text{a},n}$, due to intramolecular and intermolecular electrostatic interactions are explicitly accounted for by the first term in Eq. (4). Charge fluctuations give rise to a short-ranged attractive protein-protein interaction.^{52,53}

During the simulation, the rigid protein molecules were subjected to combined mass-center translations and rotations

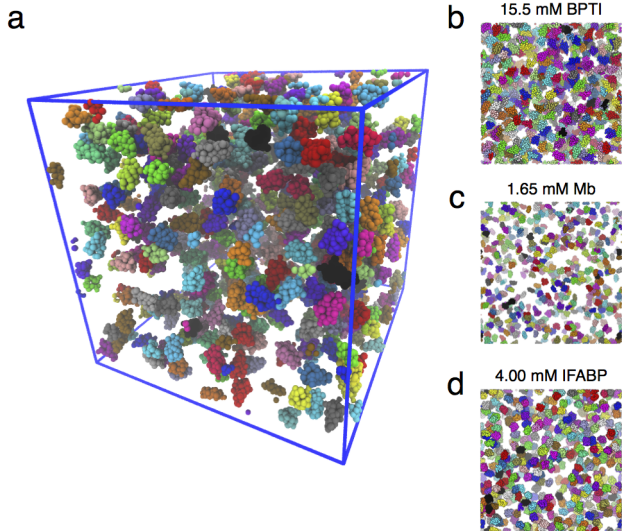


Figure 2. Snapshots from MC simulations. (a) 500 BPTI molecules (30 000 interaction sites) in a cubic cell at $C_P = 15.5$ mM. (b)–(d) Side-view of the most concentrated solution simulated for each protein (Table 2).

(25 000 moves per protein molecule), while the protonation state of all ionizable residues were alternated between protonated and deprotonated forms (20 000 moves per protein molecule). Each production MC run was preceded by a ten-fold shorter equilibration run. From the MC-generated ensemble of equilibrium configurations, we computed the average net protein valency, $Z_P = \langle \sum_n z_n \rangle$ (Table 2), and the isotropically averaged static structure factor, $S(q)$. The latter was computed from the Debye formula,^{42,43}

$$S(q) = 1 + \frac{2}{N_P} \left\langle \sum_{i=1}^{N_P-1} \sum_{j=i+1}^{N_P} \frac{\sin(qR_{ij})}{qR_{ij}} \right\rangle, \quad (6)$$

where the double sum runs over all unique protein mass-center separations, R_{ij} . The q range of the calculated $S(q)$ is limited to > 0.5 nm⁻¹ due to the finite size of the simulation box.

2.4. Colloidal Interaction Models

Two colloidal interaction models were examined, both of which describe the protein as a spherical particle. In both cases, we used analytic expressions for $S(q)$ obtained from approximate but accurate solutions of the Ornstein–Zernike integral equation.¹⁷ For the hard-sphere fluid, where excluded volume is the only interaction, we used the PY approximation,^{34,35} which is virtually exact for a hard-sphere fluid at the volume fractions of interest here. The HSY fluid includes, in addition to hard-core repulsion, a screened Coulomb (Yukawa) interaction between two uniformly charged spheres. For this model, we used the MPB-RMSA,^{36,37} which yields $S(q)$ in excellent agreement with simulations (for this model) over the full parameter space.^{36,37} For convenience, we reproduce the analytic $S(q)$

expressions for these two models in Supporting Information (Secs. S1 and S2).

As in the case of the CGSB model, we did not fit any of the parameters in the colloidal interaction models. The hard-sphere diameter, σ_P , was set to 2.46, 3.46, and 3.30 nm for BPTI, Mb, and IFABP, respectively, which reproduce the actual protein volumes, V_P , of 7.79, 21.7, and 18.8 nm³, respectively, obtained from the molar mass and partial specific volume of these proteins.^{54,55} The protein volume fraction, ϕ_P , and net valency, Z_P , were set to the values given in Tables 1 and 2, respectively.

3. Results and Discussion

3.1. Structure Factor from SAXS

Excess (protein solution minus water) scattering profiles, $I(q)$, were obtained from SAXS measurements on solutions of BPTI, Mb, and IFABP at several concentrations. In Fig. 3 we have divided $I(q)$ by the protein molar concentration, C_P , to remove the trivial concentration dependence (see Eq. (1)). As expected, $I(q)/C_P$ is independent of C_P at high q , where intramolecular scattering dominates. At lower q values, $I(q)/C_P$ decreases with increasing C_P , indicating predominantly repulsive protein–protein interactions. The structure factor, $S(q)$, in Fig. 4 was obtained, as described in Sec. 2.2, by dividing $I(q)/C_P$ with the AFF, also shown in Fig. 3.

Under certain solution conditions (high pH, high salt concentration), BPTI exists in an equilibrium between monomeric and decameric forms.^{56,57} Since the pronounced minima at $q = 1.5$ and 2.9 nm⁻¹ in the decamer form factor^{38,56} are not evident in our SAXS profiles (Fig. 3a), we conclude that decamers are not present in our BPTI solutions. The large intensity increase at $q \lesssim 0.2$ nm⁻¹ seen in all IFABP profiles (Fig. 3c) can be explained by a small fraction ($\sim 10^{-5}$) of protein in large aggregates (effective diameter $\sim 10 \times \sigma_P$). Rather than treating this structural heterogeneity explicitly, we incorporate the aggregate contribution in the AFF. To the extent that aggregation is concentration-dependent, this procedure may introduce artifacts in $S(q)$ at $q \lesssim 0.2$ nm⁻¹. Apart from this anomaly in the IFABP profiles, the AFFs for all three proteins agree well with the form factors computed with the CRY SOL program⁵⁸ from the corresponding crystal structures (Fig. 1).

3.2. Structure Factor from CGSB Model

Figure 4 also shows the structure factor predicted by the CGSB interaction model. This structure factor was computed from MC simulations at the experimental temperature, pH, and protein concentrations and with the structural model parameters determined by the protein crystal structures (Fig. 1). The only parameter that is not fixed by the protein structure is the LJ well depth

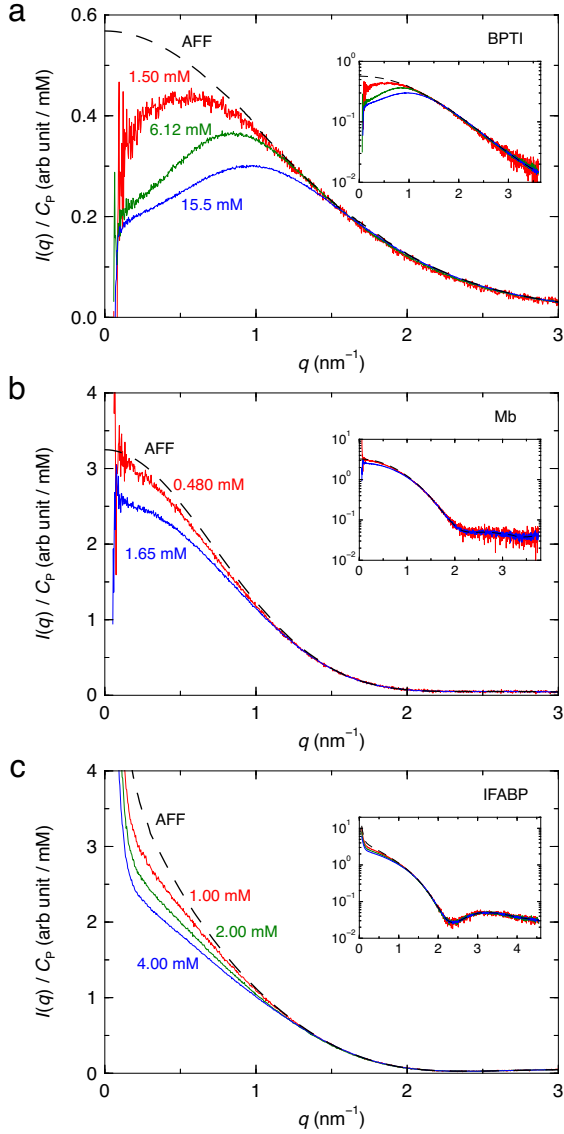


Figure 3. Concentration-normalized SAXS profiles from solutions of BPTI (a), Mb (b), and IFABP (c) at different concentrations (solid curves). Also shown is the AFF for each protein (dashed curve). The insets show the same data in semilog format.

ε (see Eq. (4)). Nominally, this parameter measures the strength of the average residue-residue vdW attraction across the aqueous solvent, but, in practice, it may also subsume short-range solvation-related interactions that are not explicitly accounted for in the CGSB model. For the CGSB calculations shown in Fig. 4, we have set $\varepsilon = 0.005 k_B T$, corresponding to a negligibly weak apparent vdW interaction. (We cannot set $\varepsilon = 0$ since this parameter also scales the steep repulsive term in Eq. (4), which is essentially determined by the vdW contact separations, σ_{ij} .)

The qualitative, and in some cases semi-quantitative, agreement found, in the q range ($> 0.5 \text{ nm}^{-1}$) accessed

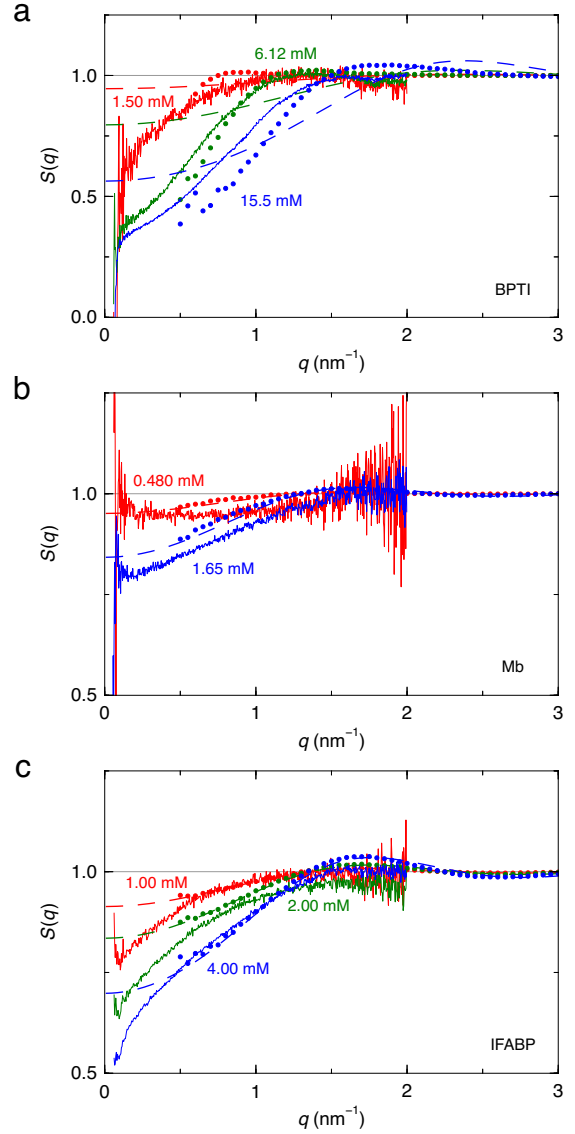


Figure 4. Structure factor for BPTI (a), Mb (b), and IFABP (c) solutions at several concentrations, obtained from SAXS experiments (solid curves), from the CGSB model without vdW attraction (dots), and from the hard-sphere model (dashed curves). The experimental $S(q)$ is only shown up to $q = 2 \text{ nm}^{-1}$; at higher q the noise amplitude exceeds any deviation from $S(q) = 1$.

by the MC simulations, between the structure factors predicted by the CGSB model with $\varepsilon = 0.005 k_B T$ and measured by SAXS (Fig. 4) indicates that the solution structure can be fairly well described by an interaction model that only incorporates excluded volume and screened inter-residue Coulomb interactions. In other words, the vdW attraction and other short-range soft interactions are either individually negligibly weak or tend to cancel out. A tenfold increase of the vdW attraction to $\varepsilon = 0.05 k_B T$, as used in previous applications of the CGSB model,^{28,30,59,60} has little effect on $S(q)$ at $q > 0.5 \text{ nm}^{-1}$ for the two proteins (BPTI and

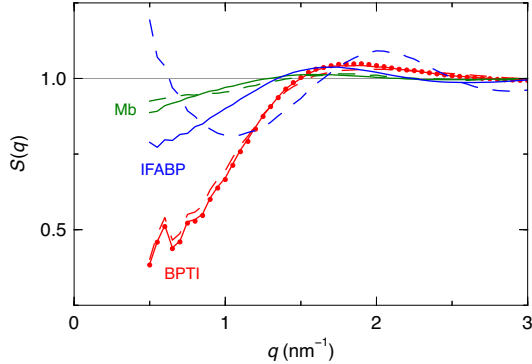


Figure 5. Structure factor predicted by the CGSB model for BPTI, Mb, and IFABP at the highest concentrations in Table 2 and with ($\varepsilon = 0.05 k_B T$, dashed curves) or without ($\varepsilon = 0.005 k_B T$, solid curves) vdW attraction. Also shown is $S(q)$ for BPTI from a simulation with fixed charges and no vdW attraction (dots).

Mb) with significant net charge (Fig. 5). In contrast, a large effect is seen for IFABP (Fig. 5), likely because the electrostatic repulsion close to the isoelectric pH (Table 2) is so weak that the protein molecules come into vdW contact more frequently.

The MC simulations with the CGSB model were carried out at constant pH. The protonation state of ionizable residues therefore undergoes thermal fluctuations and responds to the local electrostatic potential produced by charged residues in the same protein molecule and in nearby protein molecules. However, even for BPTI, which was studied at a pH where charge fluctuations are large (close to the pK_a of carboxyl groups), the attractive electrostatic interaction produced by charge fluctuations^{52,53} has negligible effect on the structure factor (Fig. 5). For Mb and IFABP, which were studied near neutral pH where charge fluctuations are less pronounced, the effect of charge fluctuations on $S(q)$ should be even smaller.

In the fluctuating-charge CGSB model, the protonation state of ionizable residues is affected by intramolecular and intermolecular electrostatic interactions. For all three proteins, the net protein charge, Z_P , computed from this model (Table 2) is within one unit from the Z_P value obtained with experimental pK_a values (Table 1). We find that Z_P depends weakly on protein concentration (Table 2). It might be expected that $|Z_P|$ should decrease in response to the increasing intermolecular electrostatic repulsion at higher protein concentration. But the opposite observed trend is due to the more effective screening of intramolecular electrostatic repulsion at higher protein concentration (the Debye screening length, κ^{-1} , is controlled by the counterions).

3.3. Structure Factor from Colloidal Models

The preceding analysis with the CGSB interaction model indicates that the structure factor is governed mainly by excluded volume and screened electrostatic interactions. To assess the importance of the irregular shape and the inhomogeneous charge distribution of the proteins, we consider two colloidal models where the protein is described as a sphere. These models are conceptually simple and computationally convenient since $S(q)$ can be expressed in analytic form (see Secs. S1 and S2 in Supporting Information).

The first model is the hard-sphere fluid, where the only interaction is the hard-core repulsion and the diameter, σ_P , of the spherical protein is fixed by the requirement that the sphere has the same volume as the real protein (see Sec. 2.4). For IFABP the structure factor predicted by the hard-sphere model is virtually identical to that obtained with the CGSB model in the q range accessed by the MC simulations (Fig. 4c). For Mb the agreement between the two models is also good, although the hard-sphere $S(q)$ is slightly displaced to larger q (Fig. 4b). For BPTI, on the other hand, the predictions of the two models differ markedly (Fig. 4a).

For Mb and IFABP, the agreement between the two models indicates that shape asymmetry and charge inhomogeneity are unimportant under the examined solution conditions. All three proteins have similar (spheroid) aspect ratios of 1.5–1.6, but neither this asymmetry nor the (coarse-grained) surface roughness appears to influence $S(q)$ significantly. In contrast to this finding, model calculations of the osmotic second virial coefficient, B_{22} , for several proteins indicate that while coarse-graining at the amino acid level (as in our CGSB model) has little effect (compared to an all-atom description), a hard-sphere model (with the same volume as the real protein) underestimates B_{22} by $\sim 35\%$.⁶¹

The excellent agreement between the two models for IFABP can be further rationalized by the nearly zero net charge at the examined pH (Table 2). Thus, at least for this protein, the inhomogeneous distribution of discrete charges appears to be unimportant. Mb has a larger, but still small, net charge (Table 2), which may account for slight shift of $S(q)$ to smaller q values (corresponding to longer distances) when the longer-ranged electrostatic repulsion is accounted for (in the CGSB model). For BPTI at pH 4, where $Z_P \approx +7$, electrostatic repulsion suppresses $S(q)$ more than for hard-core repulsion alone and also shifts the onset of this suppression to smaller q values, as expected from the longer range of the electrostatic repulsion (Fig. 4a).

In a recent SAXS study of BPTI and Mb solutions, Goldenberg and Argyle found that the experimental structure factor for Mb (at pH 7) can be well described by a hard-sphere model.¹⁶ While this conforms with our findings, it should be noted that these authors fitted both the hard-sphere diameter, σ_P , and the protein vol-

ume fraction, ϕ_P , to the SAXS data. For Mb, the fit yielded $\sigma_P = 3.74$ nm,¹⁶ slightly larger than the experimentally based value of 3.46 nm used here. It should also be noted that the solvent used by Goldenberg and Argyle contained 1 M urea and 50 mM phosphate buffer.¹⁶ Also for BPTI (at pH 7 with $Z_P \approx +6$), the hard-sphere model gave reasonable fits to the SAXS data, presumably because the buffer screened out most of the electrostatic interactions.¹⁶ But the fitted hard-sphere diameter, σ_P , was found to depend strongly on the buffer type, indicating that specific ion binding affects the protein-protein interaction.¹⁶

While we cannot compare the two models below $q = 0.5$ nm⁻¹ since the MC simulations do not access this range, we can compare the hard-sphere model with the experimental structure factor. For Mb the experimental $S(q)$ is slightly smaller than for hard spheres (Fig. 4b), consistent with a modest contribution from electrostatic repulsion. The more pronounced discrepancy seen for IFABP (Fig. 4c) can hardly be attributed to electrostatic repulsion since IFABP has a smaller net charge than Mb. Possibly, the drop of $S(q)$ below $q = 0.5$ nm⁻¹ is an artifact of incorporating the effect of IFABP aggregation in the AFF (*vide supra*).

For the more highly charged protein BPTI, the $S(q)$ predicted by the hard-sphere model differs substantially from the experimental and CGSB-based structure factors (Fig. 4a). We therefore investigated another colloidal interaction model, the HSY fluid, with a screened Coulomb repulsion in addition to the hard-core repulsion. The HSY model thus includes the two dominant interactions in the CGSB model, but the protein is now described as a sphere with a uniform surface charge density. As for the other models, we do not optimize the model parameters: the net charge, $Z_P \approx +7$, and the Debye screening length, κ^{-1} , are taken from Table 2 and the diameter, $\sigma_P = 2.46$ nm, is fixed by the protein volume (see Sec. 2.4), as in the hard-sphere model. The structure factor for the HSY model is computed from the analytic MPB-RMSA integral equation approximation, which should be quantitatively accurate under our conditions.^{36,37}

As seen from Fig. 6a, the HSY model produces a too highly structured $S(q)$. In other words, the electrostatic repulsion is too strong. The agreement with the experimental $S(q)$ can be improved by reducing the net charge (Fig. 6b), but this *ad hoc* modification is difficult to justify. Since the MPB-RMSA approximation should be accurate, we conclude that the HSY model is responsible for the discrepancy. Specifically, we infer that the inhomogeneous charge distribution of the real protein produces a weaker (orientationally averaged) electrostatic repulsion than the same net charge distributed uniformly on a spherical surface. Indeed, the crystal structure of BPTI reveals a pronounced charge asymmetry, with all the negatively charged carboxylate groups confined to

one half of the molecule (Fig. 1a). For the real protein, the electrostatic interaction should therefore be attractive for certain relative orientations so that the effective orientationally averaged potential of mean force, $w(r)$, becomes less repulsive.⁶² This anisotropy of the screened electrostatic interaction should also amplify the effect on $S(q)$ of shape asymmetry by favoring close approach of two protein molecules for relative orientations with favorable electrostatic interaction. This coupling of excluded volume and electrostatic interactions in the potential of mean force, $w(r)$, may be responsible for the observed shift of $S(q)$ to smaller q (larger separations) and the suppressed peak in $S(q)$, relative to the HSY structure factor (Fig. 6). Such effects should be less pronounced for Mb and IFABP not only because they have smaller net charge, but also because the discrete charge distribution is less asymmetric than for BPTI (Fig. 1). The HSY structure factors for Mb and IFABP indeed show good agreement with the experimental and CGSB $S(q)$, to the same extent as the hard-sphere model (Fig. 4), at high q ($\gtrsim 0.5$ nm⁻¹) where the coupling effect is expected to play an important role (Fig. S1 in Supporting Information). Not surprisingly, the charge in the HSY model leads to highly repulsive interactions, as in the case of BPTI (Fig. 6a), and the model diverges from the experiment at lower q for moderately charged Mb (Fig. S1).

To examine the effect of charge and shape asymmetry on the electrostatic contribution to the potential of mean force, we performed CGSB MC simulations with only two BPTI molecules at fixed mass-center separation and at constant pH. From the sampled orientational configurations, we calculated the orientation-averaged total (residue-based) electrostatic interaction energy between the two molecules and the intermolecular ion-ion interaction energy (Fig. 7). Note that the CGSB model incorporates both charge and shape asymmetry. As seen from Fig. 7, the total electrostatic repulsion is weaker than the ion-ion repulsion at short intermolecular separations, where charge and shape asymmetry is expected to be important (*vide supra*).

4. Conclusions

From SAXS experiments at multiple protein concentrations, we have determined the structure factor for the three globular proteins BPTI, Mb, and IFABP. Information about the protein-protein potential of mean force, averaged over relative protein orientations and solvent configurations, was derived from the experimental structure factors with the aid of several interaction models. For a structure-based interaction model coarse-grained to the amino-acid residue level, we computed the structure factor by MC simulation. For the hard-sphere and HSY models, the structure factor was obtained from accurate integral equation approximations. The parame-

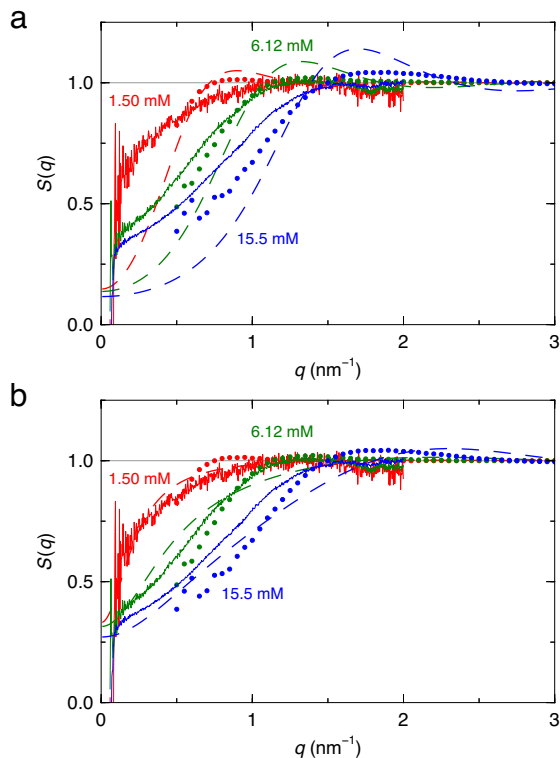


Figure 6. Structure factor for BPTI at three concentrations, obtained from SAXS experiments (solid curves), from the CGSB model without vdW attraction (dots), and from the HSY model (dashed curves). For the latter model, the net charge, Z_P , was taken from Table 2 (a) or set to +2 (b). The experimental $S(q)$ is only shown up to $q = 2 \text{ nm}^{-1}$; at higher q the noise amplitude exceeds any deviation from $S(q) = 1$.

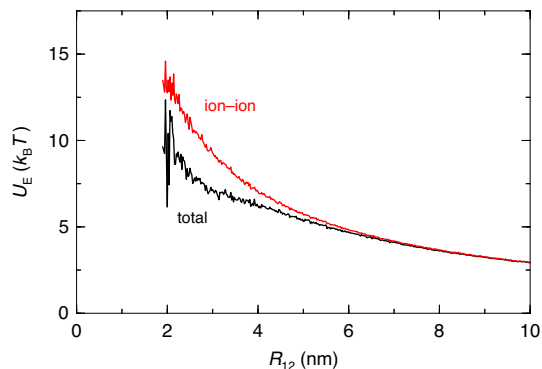


Figure 7. Orientation-averaged electrostatic energy, U_E , as a function of mass center separation, R_{12} , between two BPTI molecules evaluated exactly as $\langle \lambda_B \sum_i \sum_j z_i z_j / r_{ij} \rangle$ (black), where residues i and j belong to different molecules, and by treating the two proteins as monopoles, $\langle \lambda_B \sum_i z_i \sum_j z_j / R_{12} \rangle$ (red). The averaging was based on configurations from a two-body MC simulation at pH 4.1 and a Debye length, κ^{-1} , of 4.37 nm (*cf.* Table 2).

ters in these interaction models were fixed by the known properties of the protein solutions, rather than being optimized for agreement with the SAXS data.

For these proteins and under the investigated solution conditions, we find that the structure factor can be accounted for by excluded volume and screened electrostatic interactions, with no need to invoke other short-ranged, soft interactions, such as vdW attraction, hydrophobic and other solvent-related interactions. We cannot exclude the possibility that the effects on the structure factor of some of these apparently unimportant interactions tend to cancel out.

For Mb and IFABP, with small net charge, the structure factor is well described by a hard-sphere model, even though these proteins are non-spherical (aspect ratio 1.5–1.6) and contain many charged residues. For BPTI, with larger net charge, screened electrostatic repulsion is important, but it is weaker than predicted by a HSY model. The reduction of the electrostatic repulsion may be a result of the pronounced asymmetry of the surface charge distribution for this protein, which tends to favor protein–protein encounters with less repulsive electrostatic interactions.

The MC simulations were performed at constant pH and therefore allow for thermal fluctuations in the protonation state of ionizable residues. Such charge fluctuations do not, however, have a significant effect on the protein–protein potential of mean force under the conditions investigated here.

Acknowledgments

We thank Hanna Nilsson and Annika Rogstam (Lund Protein Production Platform) for protein preparation and purification, Marco Heinen for helpful correspondence, Bayer Healthcare AG for a generous supply of BPTI, MAX-lab for beamtime on the SAXS beamline I911-4 (proposal ID 20120020), LUNARC for computational time, and the Swedish Research Council, the Swedish Foundation for Strategic Research, Organizing Molecular Matter, eSENCE in Lund, and the Wenner-Gren Foundations for financial support.

References

- Nooren, I. M. A.; Thornton, J. M. *EMBO J.* **2003**, *22*, 3486–3492.
- Keskin, O.; Gursoy, A.; Ma, B.; Nussinov, R. *Chem. Rev.* **2008**, *108*, 1225–1244.
- Chiti, F.; Dobson, C. M. *Annu. Rev. Biochem.* **2006**, *75*, 333–366.
- Vekilov, P. G. *Soft Matter* **2010**, *6*, 5254–5272.
- George, A.; Wilson, W. W. *Acta Crystallogr.* **1994**, *D50*, 361–365.
- Zhou, H.-X.; Rivas, G.; Minton, A. P. *Annu. Rev. Biophys.* **2008**, *37*, 375–397.
- Narayanan, J.; Liu, X. Y. *Biophys. J.* **2003**, *84*, 523–532.
- Zhang, F.; Skoda, M. W. A.; Jacobs, R. M. J.; Martin, R. A.; Martin, C. M.; Schreiber, F. *J. Phys. Chem. B* **2007**, *111*, 251–259.
- Kim, S. J.; Dumont, C.; Gruebele, M. *Biophys. J.* **2008**, *94*, 4924–4931.
- Ianeselli, L.; Zhang, F.; Skoda, M. W. A.; Jacobs, R. M. J.;

- Martin, R. A.; Callow, S.; Prévost, S.; Schreiber, F. *J. Phys. Chem. B* **2010**, *114*, 3776–3783.
11. Cardinaux, F.; Zaccarelli, E.; Stradner, A.; Bucciarelli, S.; Farago, B.; Egelhaaf, S. U.; Sciortino, F.; Schurtenberger, P. *J. Phys. Chem. B* **2011**, *115*, 7227–7237.
 12. Liu, Y.; Porcar, L.; Chen, J.; Chen, W.-R.; Falus, P.; Faraone, A.; Fratini, E.; Hong, K.; Baglioni, P. *J. Phys. Chem. B* **2011**, *115*, 7238–7247.
 13. Abramo, M. C.; Caccamo, C.; Costa, D.; Pellicane, G.; Ruberto, R.; Wanderlingh, U. *J. Chem. Phys.* **2012**, *136*, 035103.
 14. Heinen, M.; Zanini, F.; Roosen-Runge, F.; Fedunová, D.; Zhang, F.; Hennig, M.; Seydel, T.; Schweins, R.; Sztucki, M.; Antalík, M.; Schreiber, F.; Nägele, G. *Soft Matter* **2012**, *8*, 1404–1419.
 15. Zhang, F.; Roosen-Runge, F.; Skoda, M. W. A.; Jacobs, R. M. J.; Wolf, M.; Callow, P.; Frielinghaus, H.; Pipich, V.; Prévost, S.; Schreiber, F. *Phys. Chem. Chem. Phys.* **2012**, *14*, 2483–2493.
 16. Goldenberg, D. P.; Argyle, B. *Biophys. J.* **2014**, *106*, 895–904.
 17. Hansen, J.-P.; McDonald, I. R. *Theory of Simple Liquids*, 2nd ed.; Academic Press: London, 1986.
 18. Louis, A. A. *Mol. Phys.* **2011**, *109*, 2945–2951.
 19. Leckband, D.; Israelachvili, J. *Q. Rev. Biophys.* **2001**, *34*, 105–267.
 20. Curtis, R. A.; Prausnitz, J. M.; Blanch, H. W. *Biotechnol. Bioeng.* **1998**, *57*, 11–21.
 21. Neal, B. L.; Asthagiri, D.; Lenhoff, A. M. *Biophys. J.* **1998**, *75*, 2469–2477.
 22. Piazza, R. *J. Cryst. Growth* **1999**, *196*, 415–423.
 23. Carlsson, F.; Malmsten, M.; Linse, P. *J. Phys. Chem. B* **2001**, *105*, 12189–12195.
 24. Grant, M. L. *J. Phys. Chem. B* **2001**, *105*, 2858–2863.
 25. Allahyarov, E.; Löwen, H.; Louis, A. A.; Hansen, J. P. *Europhys. Lett.* **2002**, *57*, 731–737.
 26. Dahirel, V.; Jardat, M.; Dufrêche, J.-F.; Turq, P. *J. Chem. Phys.* **2007**, *127*, 095101.
 27. Elcock, A. H.; McCammon, J. A. *Biophys. J.* **2001**, *80*, 613–625.
 28. Lund, M.; Jönsson, B. *Biophys. J.* **2003**, *85*, 2940–2947.
 29. McGuffee, S. R.; Elcock, A. H. *J. Am. Chem. Soc.* **2006**, *128*, 12098–12110.
 30. Persson, B. A.; Lund, M. *Phys. Chem. Chem. Phys.* **2009**, *11*, 8879–8885.
 31. Mereghetti, P.; Gabdouliline, R. R.; Wade, R. C. *Biophys. J.* **2010**, *99*, 3782–3791.
 32. Stark, A. C.; Andrews, C. T.; Elcock, A. H. *J. Chem. Theory Comput.* **2013**, *9*, 4176–4185.
 33. Quang, L. J.; Sandler, S. I.; Lenhoff, A. M. *J. Chem. Theory Comput.* **2014**, *10*, 835–845.
 34. Wertheim, M. S. *J. Math. Phys.* **1964**, *5*, 643–651.
 35. Nägele, G. *The Physics of Colloidal Soft Matter*; Institute of Fundamental Technological Research, Polish Academy of Sciences: Warsaw, 2004; Lecture Notes 14.
 36. Heinen, M.; Holmqvist, P.; Banchio, A. J.; Nägele, G. *J. Chem. Phys.* **2011**, *134*, 044532 and 129901.
 37. Heinen, M. Charged Colloids and Proteins: Structure, Diffusion, and Rheology. Ph.D. Thesis, Heinrich-Heine-Universität Düsseldorf, Germany, 2011.
 38. Kaieda, S.; Plivelic, T. S.; Halle, B. *Phys. Chem. Chem. Phys.* **2014**, *16*, 4002–4011.
 39. March, K. L.; Maskalick, D. G.; England, R. D.; Friend, S. H.; Gurd, F. R. N. *Biochemistry* **1982**, *21*, 5241–5251.
 40. Kao, Y.-H.; Fitch, C. A.; Bhattacharya, S.; Sarkisian, C. J.; Lecomte, J. T. J.; García-Moreno E., B. *Biophys. J.* **2000**, *79*, 1637–1654.
 41. Labrador, A.; Cerenius, Y.; Svensson, C.; Theodor, K.; Plivelic, T. *J. Phys. Conf. Ser.* **2013**, *425*, 072019.
 42. Guinier, A.; Fournet, G. *Small-Angle Scattering of X-rays*; Wiley: New York, 1955.
 43. *Small-Angle X-ray Scattering*; Glatter, O., Kratky, O., Eds.; Academic Press: London, 1982.
 44. Pedersen, J. S. *Adv. Colloid Interface Sci.* **1997**, *70*, 171–210.
 45. Parkin, S.; Rupp, B.; Hope, H. *Acta Crystallogr.* **1996**, *D52*, 18–29.
 46. Maurus, R.; Overall, C. M.; Bogumil, R.; Luo, Y.; Mauk, A. G.; Smith, M.; Brayer, G. D. *Biochim. Biophys. Acta* **1997**, *1341*, 1–13.
 47. Scapin, G.; Gordon, J. I.; Sacchettini, J. C. *J. Biol. Chem.* **1992**, *267*, 4253–4269.
 48. Stenqvist, B.; Thuresson, A.; Kurut, A.; Vácha, R.; Lund, M. *Mol. Simul.* **2013**, *39*, 1233–1239.
 49. Hastings, W. K. *Biometrika* **1970**, *57*, 97–109.
 50. Sassi, A. P.; Beltrán, S.; Hooper, H. H.; Blanch, H. W.; Prausnitz, J.; Siegel, R. A. *J. Chem. Phys.* **1992**, *97*, 8767–8774.
 51. Ullner, M.; Jönsson, B.; Widmark, P.-O. *J. Chem. Phys.* **1994**, *100*, 3365–3366.
 52. Kirkwood, J. G.; Shumaker, J. B. *Proc. Natl. Acad. Sci. U.S.A.* **1952**, *38*, 863–871.
 53. Lund, M.; Jönsson, B. *Q. Rev. Biophys.* **2013**, *46*, 265–281.
 54. Filfil, R.; Ratavasi, A.; Chalikian, T. V. *Biochemistry* **2004**, *43*, 1315–1322.
 55. DeMoll, E.; Cox, D. J.; Daniel, E.; Riggs, A. F. *Anal. Biochem.* **2007**, *363*, 196–203.
 56. Hamiaux, C.; Pérez, J.; Prangé, T.; Veessler, S.; Riès-Kautt, M.; Vachette, P. *J. Mol. Biol.* **2000**, *297*, 697–712.
 57. Gottschalk, M.; Venu, K.; Halle, B. *Biophys. J.* **2003**, *84*, 3941–3958.
 58. Svergun, D.; Barberato, C.; Koch, M. H. J. *J. Appl. Crystallogr.* **1995**, *28*, 768–773.
 59. Persson, B. A.; Jönsson, B.; Lund, M. *J. Phys. Chem. B* **2009**, *113*, 10459–10464.
 60. Kurut, A.; Persson, B. A.; Åkesson, T.; Forsman, J.; Lund, M. *J. Phys. Chem. Lett.* **2012**, *3*, 731–734.
 61. Grünberger, A.; Lai, P.-K.; Blanco, M. A.; Roberts, C. J. *J. Phys. Chem. B* **2013**, *117*, 763–770.
 62. Striolo, A.; Bratko, D.; Wu, J. Z.; Elvassore, N.; Blanch, H. W.; Prausnitz, J. M. *J. Chem. Phys.* **2002**, *116*, 7733–7743.
 63. Percus, J. K.; Yevick, G. J. *Phys. Rev.* **1958**, *110*, 1–13.
 64. Waisman, E. *Mol. Phys.* **1973**, *25*, 45–48.
 65. Høye, J. S.; Blum, L. *J. Stat. Phys.* **1977**, *16*, 399–413.
 66. Hayter, J. B.; Penfold, J. *Mol. Phys.* **1981**, *42*, 109–118.
 67. Cummings, P. T.; Smith, E. R. *Mol. Phys.* **1979**, *38*, 997–1001.
 68. Cummings, P. T.; Smith, E. R. *Chem. Phys.* **1979**, *42*, 241–247.
 69. Cummings, P. T.; Stell, G. *J. Chem. Phys.* **1983**, *78*, 1917–1923.
 70. Hansen, J.-P.; Hayter, J. B. *Mol. Phys.* **1982**, *46*, 651–656.
 71. Snook, I. K.; Hayter, J. B. *Langmuir* **1992**, *8*, 2880–2884.

Supporting Information

S1. Hard-Sphere Fluid

For a fluid of identical hard spheres of diameter σ , the pair interaction energy is

$$w(x) = \begin{cases} \infty & , x < 1 , \\ 0 & , x > 1 , \end{cases} \quad (\text{S1})$$

where $x = r/\sigma$ is the reduced inter-particle separation. For this model, the pair correlation function (PCF), $g(x)$, obeys the exact condition

$$g(x) = 0 , x < 1 , \quad (\text{S2})$$

which simply expresses the impenetrability of the hard spheres.

According to the Percus–Yevick (PY) approximation,⁶³ the direct correlation function, $c(x)$, is related to the PCF and the pair potential as

$$c(x) = g(x) \left\{ 1 - \exp \left[\frac{w(x)}{k_B T} \right] \right\} . \quad (\text{S3})$$

For the hard-sphere model in Eq. (S1), this implies that

$$c(x) = \begin{cases} -y(x) & , x < 1 , \\ 0 & , x > 1 , \end{cases} \quad (\text{S4})$$

where the function $y(x) \equiv g(x) \exp[w(x)/(k_B T)]$ is continuous at $x = 1$.

For the hard-sphere fluid, the approximate PY closure in Eq. (S4) allows the formally exact Ornstein–Zernike (OZ) integral equation¹⁷ to be solved analytically.³⁴ The resulting structure factor³⁵ is a function of the reduced wavevector $Q \equiv q\sigma$ and the particle volume fraction $\phi = n_P \pi \sigma^3 / 6$:

$$S(Q) = \frac{1}{|F(Q)|^2} = \frac{1}{[\text{Re } F(Q)]^2 + [\text{Im } F(Q)]^2} , \quad (\text{S5})$$

with

$$\begin{aligned} \text{Re } F(Q) &= 1 - 12\phi [a_0(\phi)G_a(Q) + b_0(\phi)G_b(Q)] , \\ \text{Im } F(Q) &= -12\phi [a_0(\phi)H_a(Q) + b_0(\phi)H_b(Q)] . \end{aligned} \quad (\text{S6})$$

Here we have defined

$$\begin{aligned} a_0(\phi) &= \frac{1 + 2\phi}{(1 - \phi)^2} , \\ b_0(\phi) &= -\frac{3\phi}{2(1 - \phi)^2} , \end{aligned} \quad (\text{S7})$$

and

$$\begin{aligned} G_a(Q) &= \frac{Q \cos Q - \sin Q}{Q^3} , \\ G_b(Q) &= \frac{\cos Q - 1}{Q^2} , \\ H_a(Q) &= \frac{Q \sin Q + \cos Q - 1 - Q^2/2}{Q^3} , \\ H_b(Q) &= \frac{\sin Q - Q}{Q^2} . \end{aligned} \quad (\text{S8})$$

This analytic result is highly accurate up to volume fractions $\phi \approx 0.35$.

S2. Hard-Sphere Yukawa Fluid

Solutions of charged colloidal particles or proteins are often modeled as a one-component macrofluid composed of charged hard spheres in a uniform neutralizing background medium. Apart from their excluded volume, the particles

are taken to interact with a screened Coulomb (Yukawa) potential, so that

$$\frac{w(x)}{k_{\text{B}}T} = \begin{cases} \infty & , x < 1 , \\ \gamma \frac{e^{-kx}}{x} & , x > 1 , \end{cases} \quad (\text{S9})$$

where $x \equiv r/\sigma$. Furthermore, γ is a dimensionless coupling constant and k is a dimensionless screening parameter. These are given by

$$\gamma \equiv \frac{\lambda_{\text{B}}}{\sigma} \frac{e^k}{(1+k/2)^2} Z^2 , \quad (\text{S10})$$

$$k^2 \equiv (\kappa\sigma)^2 = 4\pi\lambda_{\text{B}}\sigma^2(n_{\text{P}}|Z| + 2n_{\text{S}}) = \frac{\lambda_{\text{B}}}{\sigma} (24\phi|Z| + 8\pi n_{\text{S}}\sigma^3) , \quad (\text{S11})$$

where Z is the net protein charge (in units of e), n_{P} is the protein number density, $\phi = n_{\text{P}}\pi\sigma^3/6$ is the protein volume fraction, and n_{S} is the number density of monovalent salt. The number density of counterions, also assumed monovalent, is $n_{\text{P}}|Z|$. Finally, $\lambda_{\text{B}} = e^2/(4\pi\epsilon_0\epsilon_{\text{r}}k_{\text{B}}T)$ is the Bjerrum length.

For the hard-sphere Yukawa (HSY) model in Eq. (S9), the OZ equation can be solved analytically in the mean spherical approximation (MSA),^{64,65} defined by

$$c(x) = -\frac{w(x)}{k_{\text{B}}T} , \quad x > 1 , \quad (\text{S12})$$

along with Eq. (S2). Various forms of the lengthy analytic solution for the structure factor, $S(q)$, and other quantities have been published. All involve the solution of a quartic equation, but different formulations have been presented where the quartic equation takes different forms. The results of Hayter and Penfold⁶⁶ are free from misprints, but they do not provide an analytic solution of the quartic equation. Moreover, the physical root (among the four possible roots) is identified by showing that it leads to $g(x) = 0$ for $x < 1$ and this requires a numerical Fourier transform. For analysis of SAXS data, it is more convenient to use the completely analytic formulation presented by Cummings *et al.*^{37,67-69}

In this so-called Wiener–Hopf factorization approach, a complex-valued function $F(Q)$ is defined such that

$$1 - n_{\text{P}}\hat{c}(Q) = F(Q)F(-Q) = |F(Q)|^2 = [\text{Re } F(Q)]^2 + [\text{Im } F(Q)]^2 , \quad (\text{S13})$$

where $Q \equiv q\sigma$ and $F(-Q) = [F(Q)]^*$ for real Q . The structure factor, $S(Q)$, can then be expressed on the form of Eq. (S5). The function $F(Q)$ is related to the Fourier transform of another function $F(x)$:

$$F(Q) = 1 - 2\pi n_{\text{P}}\sigma^3 \int_{-\infty}^{\infty} dx e^{iQx} F(x) = 1 - 12\phi \int_{-\infty}^{\infty} dx e^{iQx} F(x) . \quad (\text{S14})$$

For the HSY model in the MSA approximation, the function $F(x)$ is given by⁶⁹ (but Cummings' earlier papers^{67,68} give this function incorrectly)

$$F(x) = \begin{cases} 0 & , x < 0 , \\ F_0(x) + \beta e^{-k(x-1)} & , 0 \leq x < 1 , \\ \beta e^{-k(x-1)} & , x \geq 1 , \end{cases} \quad (\text{S15})$$

where k is defined by Eq. (S11) and

$$F_0(x) = \frac{a}{2}(x^2 - 1) + b(x - 1) + d\beta[1 - e^{-k(x-1)}] . \quad (\text{S16})$$

The quantities a , b , d , and β are functions of the system parameters γ , k , and ϕ .

Combining Eqs. (S14)–(S16) and performing the integral, one obtains

$$\begin{aligned} \text{Re } F(q) &= 1 - 12\phi \left[aG_a(Q) + bG_b(Q) + \frac{\beta U(Q)}{(k^2 + Q^2)} \right] , \\ \text{Im } F(q) &= -12\phi \left[aH_a(Q) + bH_b(Q) + \frac{\beta V(Q)}{(k^2 + Q^2)} \right] , \end{aligned} \quad (\text{S17})$$

where the functions $G_a(Q)$, $G_b(Q)$, $H_a(Q)$, and $H_b(Q)$ are given by Eq. (S8) and

$$\begin{aligned} U(Q) &= dk \left[\cos Q + k \frac{\sin Q}{Q} \right] - (d-1)ke^k, \\ V(Q) &= dk \left[\sin Q - k \frac{(\cos Q - 1)}{Q} \right] + Q[d - (d-1)e^k]. \end{aligned} \quad (\text{S18})$$

The quantities a and b are given by^{37,67,68}

$$a = a_0 + \frac{12\phi\beta}{k(1-\phi)^2} [3d\phi k - \omega\tau], \quad (\text{S19})$$

$$b = b_0 + \frac{12\phi\beta}{k(1-\phi)^2} \left[(1-4\phi)\frac{kd}{2} + \omega\rho \right], \quad (\text{S20})$$

with a_0 and b_0 as defined in Eq. (S7), and

$$\omega = d(1+k) - (d-1)e^k, \quad (\text{S21})$$

$$\tau = 1 + 2\phi - \frac{6\phi}{k}, \quad (\text{S22})$$

$$\rho = \frac{3\phi}{2} + \frac{(1-4\phi)}{k}. \quad (\text{S23})$$

The dependence on the coupling constant γ enters via the quantity

$$d = \frac{(\beta D + K)e^{-k} + \beta^2 E}{\beta^2 F}, \quad (\text{S24})$$

which involves the additional quantities

$$D = k - a_0 P - b_0 T, \quad (\text{S25})$$

$$E = -6\phi + \delta(\tau P - \rho T), \quad (\text{S26})$$

$$F = -6\phi(1 - e^{-k})^2 + P\delta[\mu\tau + 3\phi ke^{-k}] - T\delta\left[\mu\rho - \frac{1}{2}(1-4\phi)ke^{-k}\right], \quad (\text{S27})$$

where

$$\delta = \frac{12\phi}{k(1-\phi)^2}, \quad (\text{S28})$$

$$\mu = 1 - (1+k)e^{-k}, \quad (\text{S29})$$

$$P = 12\phi \left(\frac{\mu}{k^2} - \frac{1}{2} \right), \quad (\text{S30})$$

$$T = \frac{12\phi}{k} (1 - k - e^{-k}), \quad (\text{S31})$$

and the (non-negative) coupling strength parameter

$$K = \gamma e^{-k}. \quad (\text{S32})$$

Finally, β is one of the four roots of the quartic equation

$$36\phi^2\beta^4 - 6\phi X\beta^3 - 12\phi K\beta^2 + KY\beta + K^2 = 0, \quad (\text{S33})$$

where

$$\begin{aligned} X &= ke^{-k} - \frac{6\phi}{(1-\phi)k^2} [2 - 2k - (2 - k^2)e^{-k}] - W, \\ Y &= k - \frac{6\phi}{(1-\phi)k^2} [2 - k^2 - 2(1+k)e^{-k}] - W, \\ W &= \frac{18\phi^2}{(1-\phi)^2 k^2} [2 - k - (2+k)e^{-k}]. \end{aligned} \quad (\text{S34})$$

The desired root reduces to the PY solution in the limit $K \rightarrow 0$ and in the limit $\phi \rightarrow 0$ it yields^{67,68}

$$\beta = -\frac{K}{k}[1 + \mathcal{O}(\phi)] . \quad (\text{S35})$$

We obtain the following analytic expression for the desired root:

$$\begin{aligned} \beta &= \frac{X}{24\phi} + \frac{\sqrt{B_2} - \sqrt{B_1}}{2} , \\ B_1 &= \Gamma + \Lambda , \\ B_2 &= 2\Gamma - \Lambda - \frac{1}{18\phi^2\sqrt{B_1}} \left[K(X - Y) + \frac{X^3}{48\phi} \right] , \\ \Gamma &= \left[\frac{X}{12\phi} \right]^2 + \frac{2K}{9\phi} , \\ \Lambda &= \frac{R}{(6\phi)^2} + C , \\ C &= \frac{K(32K\phi + XY)}{18\phi R} , \\ R &= \left\{ 2K\phi^2 \left[M - \left(\frac{KL}{\phi} \right)^{1/2} \right] \right\}^{1/3} , \\ M &= (16K)^2\phi + 3K(3X^2 + 3Y^2 - 2XY) , \\ L &= 2[48K\phi(X - Y)]^2 - 2(XY)^3 \\ &\quad + 3K\phi \left[2(XY)^2 + 9(3X^4 - 4X^3Y - 4XY^3 + 3Y^4) \right] . \end{aligned} \quad (\text{S36})$$

Apart from the errors^{67,68} in $F(x)$ noted above, the literature contains several other misprints in the analytic MSA result. Cummings & Smith in their Molecular Physics paper⁶⁷ have a sign error in W (their Eq. (6a)), defined here in Eq. (S34), and in their Chemical Physics paper⁶⁸ they omit a factor $\exp(k)$ in the definition of b (their Eq. (9b)). Marco Heinen in his PhD thesis³⁷ (Appendix A) has misprints in the second lines of his Eqs. (A.2) and (A.3) (which define $\text{Re } F(q)$ and $\text{Im } F(q)$), where b appears in place of k . Heinen also introduces a quantity f , which is unnecessary since $f = (1 - d) \exp(k)$. Furthermore, all other authors define K with the opposite sign to that in Eq. (S32).

The MSA solution of the HSY model is accurate (as compared to Monte Carlo simulations of the same model) for weakly charged macroions at relatively high volume fractions. But for highly charged macroions and/or at low volume fractions, the MSA produces unphysical results. Specifically the contact PCF, $g(\sigma)$, becomes negative. Various schemes have been proposed to improve the MSA. The basic idea is that, under the conditions where the MSA fails, the macroions are almost always so far apart (because the volume fraction is low and/or because of strong electrostatic repulsion) that the actual hard-sphere diameter σ has no effect on $S(q)$. It is therefore possible to increase σ to a larger value σ' so that $g(\sigma)$ remains non-negative. Specifically, σ' is chosen so that $g(\sigma'; \phi') = 0$, where $\phi' = \phi(\sigma'/\sigma)^3$ is the rescaled volume fraction. (The volume fraction increases because the particle size is increased at constant particle number density n_p .) This approach is called the rescaled MSA (RMSA).⁷⁰

Comparison with computer simulations shows that even the RMSA is not accurate for strongly repulsive macroions (high charge and/or low salt concentration). In particular, the RMSA tends to underestimate the local ordering by yielding a too small principal peak in $S(q)$ (and in $g(r)$) and a too large osmotic compressibility, $S(0)$. It was shown that the accuracy of the RMSA can be further improved by redefining the model parameters γ and k to correct for the fact that the counterions are treated in the one-component macrofluid model (of which the HSY model is a special case) as a uniform background medium that penetrates the macroion and therefore reduces its effective charge. This scheme is called the penetrating-background corrected RMSA (PB-RMSA).⁷¹ A further improvement, yielding a structure factor, $S(q)$, in excellent agreement with Monte Carlo simulations in the full parameter space, was obtained with a modified PB-RMSA (MPB-RMSA) scheme.³⁶ This MPB-RMSA scheme involves the following steps:³⁶

- (1) Specify the true model parameters σ , ϕ , γ , and k , with γ given by Eq. (S10) and k by the following modified version of Eq. S11:

$$k^2 = \frac{\lambda_B}{\sigma(1 - \phi)} (24\phi|Z| + 8\pi n_S \sigma^3) . \quad (\text{S37})$$

(2) Compute the modified parameters:

$$\begin{aligned} k_{\text{mod}} &= k(1 - \phi)^{1/2} , \\ \gamma_{\text{mod}} &= \gamma \exp(k_{\text{mod}} - k) \left(\frac{1 + k/2}{1 + k_{\text{mod}}/2} \right)^2 . \end{aligned} \quad (\text{S38})$$

(3) Assign the further modified parameters:

$$\begin{aligned} k^* &= k_{\text{mod}} - 2\phi^{1/3} \ln(1 - \phi) , \\ \gamma^* &= \frac{\gamma_{\text{mod}}}{(1 - \phi)^2} . \end{aligned} \quad (\text{S39})$$

(4) The contact PCF is given by³⁷

$$\begin{aligned} g_0 \equiv g(\sigma) &= a(1 + \beta P) + b(1 + \beta T) - K + \beta k(d - 1) \\ &\quad - 6\phi\beta^2 [2d(\cosh k - 1) - e^k] . \end{aligned} \quad (\text{S40})$$

Using this result, compute $g_0(\phi, \gamma^*, k^*)$, that is, the contact PCF with modified Yukawa parameters. If $g_0 < 0$, assign an initial rescaling parameter $s = 0.99$ and go to step 5. If $g_0 \geq 0$, set $\sigma^* = \sigma$ and $\phi^* = \phi$ and go to step 7.

(5) Compute the rescaled parameters:

$$\begin{aligned} \sigma^* &= \frac{\sigma}{s} , \\ \phi^* &= \frac{\phi}{s^3} , \\ \gamma^* &= \frac{\gamma_{\text{mod}} s}{(1 - \phi^*)^2} , \\ k^* &= \frac{k_{\text{mod}}}{s} - 2(\phi^*)^{1/3} \ln(1 - \phi^*) . \end{aligned} \quad (\text{S41})$$

(6) Using Eq. (S40), compute $g_0(s) \equiv g_0(\phi^*, \gamma^*, k^*)$, that is, the contact PCF with rescaling parameter s . If $|g_0(s)| < \text{tol}$, go to step 7. Here tol is a tolerance parameter with default value 10^{-6} . If $|g_0(s)| \geq \text{tol}$, compute a new rescaling parameter s' that yields a $g_0(s')$ closer to 0. This is accomplished by iteratively solving the equation $g_0(s') = 0$ with the Newton–Raphson algorithm:

$$s' = s - g_0(s) \left[\frac{dg_0(s)}{ds} \right]^{-1} . \quad (\text{S42})$$

Then set $s = s'$ and go to step 5.

(7) Compute the structure factor, $S(q)$, in the desired q range by using Eqs. (S5), (S7), (S8), (S17)–(S32), and (S36) and the input parameters $Q^* = q\sigma^*$, ϕ^* , γ^* , and k^* .

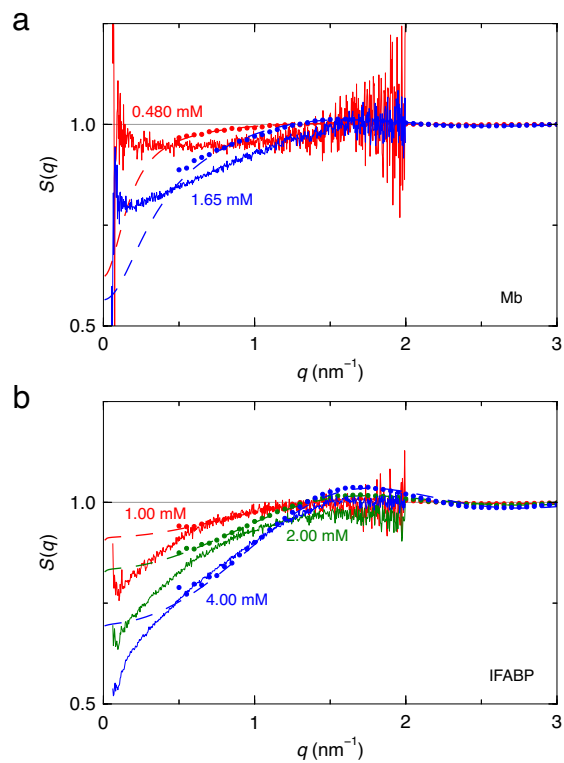


Figure S1. Structure factor for Mb (a) and IFABP (b) solutions at multiple concentrations, obtained from SAXS experiments (solid curves), from the CGSB model without vdW attraction (dots), and from the HSY model (dashed curves). For the HSY model, the net charge, Z_P , was taken from Table 2. The experimental $S(q)$ is only shown up to $q = 2 \text{ nm}^{-1}$; at higher q the noise amplitude exceeds any deviation from $S(q) = 1$.